Cold Regions Science and Technology 242 (2026) 104762

Contents lists available at ScienceDirect

Cold Regions Science and Technology

journal homepage: www.elsevier.com/locate/coldregions

Active layer modelling at Stelvio Pass, Italian Alps☆

Vasudha Chaturvedi [a,b], Stefano Ponti [a,c,*], Mauro Guglielmin [a,c]

[a] Department of Theoretical and Applied Sciences, University of Insubria, via J. H. Dunant, 3, 21100 Varese, Italy
[b] University School for Advanced Studies (IUSS) Pavia, p.zza della Vittoria, 15, 27100 Pavia, Italy
[c] Climate Change Research Center (CCRC), University of Insubria, via Sant'Abbondio, 12, 22100 Como, Italy

ARTICLE INFO

Keywords:
Permafrost modelling
Active layer thickness
Alpine permafrost
PERMACLIM
Ground surface temperature

ABSTRACT

Here, we present the result of different models for active layer thickness (ALT) in an area of the Italian Central Alps where a few information about the ALT is present. Looking at a particular warm year (2018), we improved PERMACLIM, a model used to calculate the Ground Surface Temperature (GST) and applied two different versions of Stefan's equation to model the ALT. PERMACLIM was updated refining the temporal basis (daily respect the monthly means) of the air temperature and the snow cover. PERMACLIM was updated also to minimize the bias of the snow cover in summer months using the PlanetScope images. Moreover, the contribution of the solar radiation was added to the air temperature to improve the summer GST. The modelled GST showed a good calibration and, among the two versions of Stefan's equation, the first (ALT1) indicates a maximum active layer thickness of 7.5 m and showed a better accuracy with R2 of 0.93 and RMSE of 0.32 m. The model underlined also the importance of better definition of the thermal conductivity of the ground that can strongly influence the ALT.

1. Introduction

1.1. Permafrost and climate change

Among the "hotspots" of the mountain areas, warming of Alps is greater than hemispherical or global scale average (Malfasi and Cannone, 2021). Climate sensitivity of the Alps affects the underlying conditions of permafrost, its degradation and thickening of active layer which would cause feedback such as ground instability, ecosystem and hydrological changes (Cannone and Sgorbati, 2007; Gruber and Haeberli, 2007; Woo et al., 2008; Schuur et al., 2015; Ponti et al., 2021; Wani et al., 2021). Permafrost degradation induces the increasing of the active layer thickness (ALT) and alters vegetation, decomposition of organic carbon in the soil, fluxes of greenhouse gases, moisture content, and infrastructure (Jiang et al., 2024; Liu et al., 2024; Wu et al., 2024). ALT can vary substantially over small regions because of differences in energy balance due to the high variability of surface characteristics as snow, vegetation and ground characteristics as thermal properties and soil moisture (Fisher et al., 2016; Yi et al., 2019; Song et al., 2020; Heijmans et al., 2022). It is therefore important to rely on high resolution data that represent the complex variability of the environment for modelling permafrost conditions and its changing dynamics, coupled with field-based observation (Wang et al., 2020).

1.2. Permafrost modelling

Modelling the surface energy balance (SEB) coupling with ground thermal conditions and characteristics is still a challenge to overcome (Hoelzle et al., 2001; Guglielmin and Testa, 2003). Indeed, the current spatial resolution of permafrost and active layer maps produced for hemispherical scale studies do not represent the true surface spatial variability (Ran et al., 2022). Therefore, there is still a need of fine-resolution maps that capture the local heterogeneity. Many studies have been conducted on ALT modelling with analytic, direct, indirect, and numerical models. The analytical equation of Kudryavtsev is a complex model requiring integrative information on many variables such as snow cover, snow density, vegetation, thermal properties of soil in frozen and thawed state. Moreover, the assumptions of heat flux overestimates ALT (Riseborough et al., 2008; Li et al., 2022). The subsurface thermal model CryoGrid3 uses many variables and is driven by time series. It assumes a constant density of snow; energy transfer is estimated using low-vegetated areas and water level changes are considered constant throughout all seasons (Westermann et al., 2016). The numerical model GIPL2-MPL input parameters are spatial datasets

☆ This article is part of a Special issue entitled: 'Permafrost' published in Cold Regions Science and Technology.

* Corresponding author at: Department of Theoretical and Applied Sciences, University of Insubria, via J. H. Dunant, 3, 21100 Varese, Italy.
E-mail address: stefano.ponti@uninsubria.it (S. Ponti).

https://doi.org/10.1016/j.coldregions.2025.104762
Received 30 May 2025; Received in revised form 3 November 2025; Accepted 19 November 2025
Available online 25 November 2025

such as precipitation, air temperature, ground water content, thermal properties of soil and five downscaled IPCC Global Circulation Models. However, the model has high precipitation bias, insufficient long-term data for the model's comprehensive analysis and soil moisture, snow depth and snow thermal properties require further improvement (Jafarov et al., 2012). It is for this reason that the increase of ground-based and high resolution remotely sensed observations, would lead to developments in permafrost mapping and variability representation (Ran et al., 2022; Ponti et al., 2024).

At local scale, in the Alps, mountain permafrost modelling has been conducted from topographic factors and air temperatures (PERMAKART, Keller, 1992) and from heat fluxes estimations (PERMEBAL, Stocker-Mittaz et al., 2002) or a combination of both (PERMACLIM, Guglielmin and Testa, 2003). More recently, the Alpine Permafrost Index Map (APIM) (Boeckli et al., 2012) has been developed, but on an old climatic series. It is for these reasons that there is a need to update such local permafrost models to best represent the high spatial variability of alpine regions with recent and representative climatic series. Guglielmin et al. (2022) performed such update at Mt. Foscagno area, but a simplification of PERMACLIM model is needed to make it reusable over larger areas with a set of easily accessible input variables.

Therefore, here we believe that an upgrade together with a simplification of PERMACLIM would be suitable to model the ground surface temperature (GST) at high spatio-temporal resolution. Respect to the original model, we aim to improve significantly the temporal resolution of the climatic linear regressions (air temperature and snow thickness) from monthly to daily. Secondly, we also modify the model by using satellite snow coverage in late spring, summer and in early autumn periods, while snow thickness in the winter period through linear regressions lapse-rate. Through the modelling of GST, this paper aims mainly to assess the ALT in a particularly warm year (2018) as indicator of extreme deepening of the permafrost table and thus a possible example of the warmer future years in one selected area (Stelvio Pass area) where important infrastructure exists and within a biodiversity hotspot in one of the oldest Italian National Park. Moreover, the simplicity and reliability of the twopresented versions of this model would make it easily reproducible and give future users a quantification of errors in order to choose the best way to approach ALT modelling depending on the available input data. This would be of interest not only to researchers but also to public agencies responsible for the proper management of high-elevation infrastructure (Mourey et al., 2019; Hjort et al., 2022).

2. Study area

The study area lies in the patchy and discontinuous permafrost zone of Stelvio National Park close to Stelvio Pass (46°31′ N, 10°25′ E) (Fig. 1). Approximately 1.6 km on the eastern side of the study area lies the SHARE STELVIO Borehole (SSB) world's deepest borehole in the mountain permafrost with a depth of 235 m and a permafrost thickness

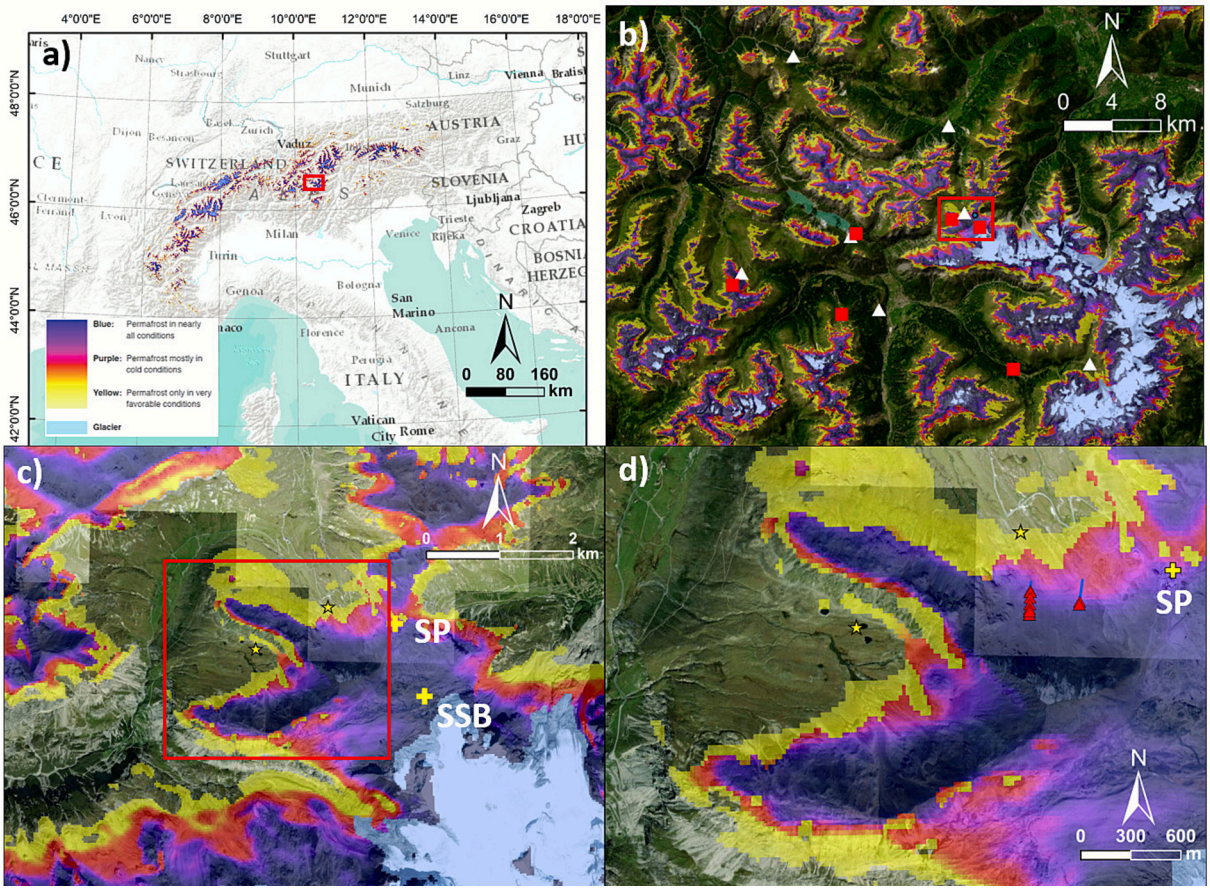

Fig. 1. Study area and alpine permafrost index map (APIM) distribution (Boeckli et al., 2012). a) location of the study area in the European Alps hill shade, b) zoomed in view of study area in the Italian Central Alps: Automatic weather stations (AWSs) location used in this study for snow thickness (white triangles) and air temperature (red quadrats); c) satellite imagery highlighting study area in red square: yellow crosses represent the location of 1) SP = Stelvio Pass, 2) SSB = Share Stelvio Borehole; d) satellite image overview of the area of interest: blue lines represent electric resistivity tomography (ERT) profiles carried out over a ski run (right) and an active rock glacier (left), red triangles indicate validation points of ERT profiles used for the ALT calibration. Yellow stars locate the observed ground locations for GST used for validation (ITEX Stelvio Pass) and (ITEX Scorluzzo). ITEX = international tundra experiment. (For interpretation of the references to colour in this figure legend, the reader is referred to the web version of this article.)

exceeding 235 m. (Guglielmin et al., 2018). Here, permafrost warmed of 0.2 °C during 2009–2016 (Biskaborn et al., 2019) and ALT is increasing of 70 cm per decade (Etzelmüller et al., 2020). The elevation ranges from 1956 to 3100 m a.s.l and it is mainly characterised by lithologies as dolostone, paragneiss and granitic orthogneiss. The whole area is characterised by glacial Holocenic features and periglacial landforms (Guglielmin et al., 2001, 2018). In particular, among the periglacial features, scree slopes, pattern grounds, solifluction lobes, protalus ramparts, debris flows are widespread and also two active rock glaciers occur (Cannone et al., 2003; Ponti et al., 2021). The mean annual air temperature (1978–2018) based on the closest meteorological station located at Cancano (46°31′02.2″ N, 10°19′14.7″ E, 1948 m a.s.l) is +3.3 °C ± 0.8 °C, with mean annual precipitation of 817 mm and snowfall reaching maximum thickness of 133 cm (Malfasi and Cannone, 2021; Ponti et al., 2021).

The vegetation encompasses subalpine, alpine, and nival belts ranging from 2000 to 2800 m a.s.l. The alpine belt mostly consists of climax alpine grasslands/continuous meadows (*Caricetum curvulae*) and *Salicetum herbaceae* in snow beds. The subalpine belt dominates with dwarf shrubs, while the nival belt is colonized by pioneer vegetation (*Androsacetum alpinae, Oxyrietum digynae,* and *Luzuletum spadiceae*), snow bed communities and barren ground.

Anthropogenic impacts in the study area are the extensive summer pasturing, walking trails used by the hikers and the ski run which was built destroying a rock glacier in 1987 (Cannone et al., 2003; Malfasi and Cannone, 2020; Guglielmin et al., 2021).

3. Input data

3.1. Surface data

The digital elevation model (DEM) was downloaded by *https://www.geoportale.regione.lombardia.it/* and it has a 5 m spatial resolution. The slope and curvature were computed using ArcGIS Pro 2.7 spatial analyst tool. The slope values ranged from 0 to 82° with the highest values denoting the steepest slopes of rock walls and vertical cliffs. Curvature values lie within −463 to 373 with negative values indicating a convex surface, positive values showing a concave surface, and values of 0 representing a surface that is flat.

The geological map (Montrasio et al., 2012) surveyed at 1:10.000 (that is the best resolution available for a detailed geological mapping in Italy) was re-classified to highlight bedrock and deposits and define their thermo-physical properties. Blocky gravel sand without soil is the most extensive type followed by sand gravel with soil.

3.2. Climate data

Among the available data (2016–2021) we selected the 2018 because, as shown in Fig. 2, summer and early fall monthly thawing degree days (TDD) of air and GST were warmer than the others with an earlier onset of summer temperatures and a delayed decrease of positive temperature values. This represents an extreme deepening of the AL and thus, if the same conditions are maintained in future, a consequent deepening of the permafrost table.

Daily mean air temperature and snow cover thickness derived from the Automatic Weather Stations (AWS) available in the area and located in Fig. 1b.

We used 6 AWSs for air temperature (AT) in 2018 (ITEX Stelvio Pass at 2612 m a.s.l, ITEX scorluzzo at 2630 m a.s.l, Cancano at 1935 m a.s.l, Oga S. Colombano at 2300 m a.s.l, La Vallaccia at 2648 m a.s.l, S. Caterina at 1761 m a.s.l (Fig. 1b). The data for AWS were downloaded from *https://www.arpalombardia.it*.

Snow cover presence and thickness were measured at 7 AWSs (Fig. 1b). Four of them were the same used for air temperature (Cancano, Oga S. Colombano, Vallaccia, ITEX while other three (Forni at 2181 m a.s.l., Buffalora at 1971 m a.s.l and Santa Maria Val Mustair at 1386 m a.s.l) were added.

3.3. Field data

37 points monitoring the ground surface temperature (GST, measured at 2 cm of depth through Onset Hobo U23, accuracy of 0.2 °C) were considered in the locations named ITEX Scorluzzo and ITEX Stelvio Pass with an elevation ranging between 2608 and 2635 m a.s.l. (Fig. 3).

Soil moisture was calculated from soil samples collected in 36 points located in different types of deposits in all the study area between an altitude of 2200 and 2700 m a.s.l. Water content was calculated with weight loss by oven-drying the soil at 105 °C for 24 h (Gardner, 1986) and averaged for the different horizons examined in each soil. The measured values range between 14 and 54 % depending upon the soil

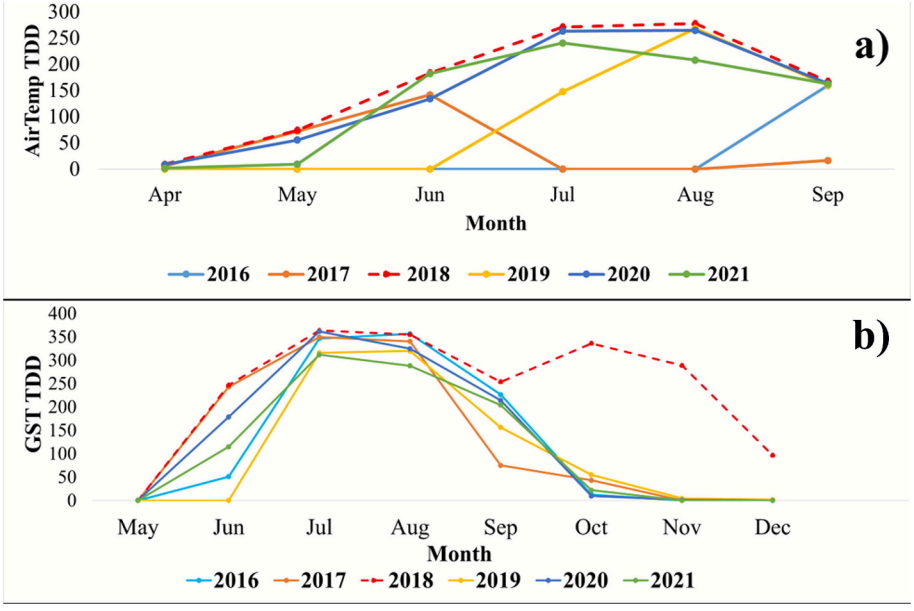

Fig. 2. Monthly thawing degree days (TDD, °C day) of: a) Air temperature between April and September and b) GST for the months May–December of ITEX Stelvio Pass station for the year 2016, 2017, 2018, 2019 and 2021.

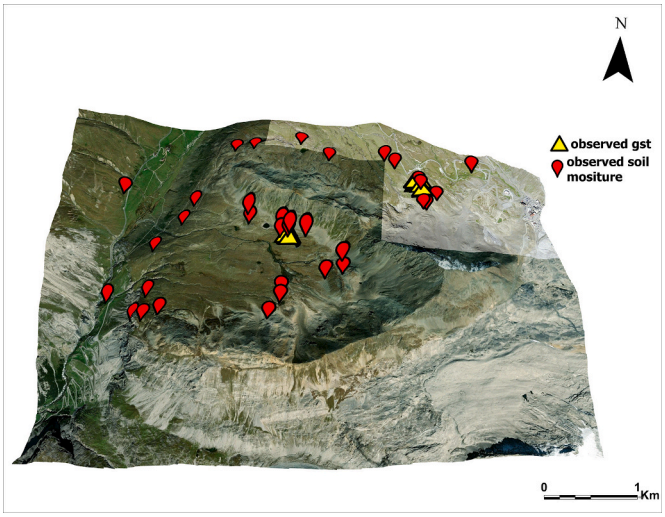

Fig. 3. Locations of ground surface temperature and soil moisture points in the study area at Stelvio Pass. GST points are coloured in yellow and soil moisture in red. (For interpretation of the references to colour in this figure legend, the reader is referred to the web version of this article.)

density and porosity (Fig. 3). For the validation of ALT, nine chosen points on two different electrical resistivity tomography (ERT) surveys (235 m and 94 m long) were considered to detect ALT as the depth of a high resistivity layer, corresponding to a high ice-content layer (permafrost table). The ERTs were taken in August 2018 (almost maximum ground thawing) with a Wenner array geometry and an electrode spacing of 5 and 2 m, respectively. Res2Dinv software was used to invert the data, setting a root mean square (RMS) convergence limit equal to 5 % (Guglielmin et al., 2021).

4. Methods

4.1. GST model

The GST of 2018 was modelled with an updated version of the PERMACLIM (Fig. 4) (Guglielmin and Testa, 2003). The first improvements were that the air temperature maps were calculated on daily basis and not on monthly as in PERMACLIM. All the linear regressions lapse-rate between air temperature and elevation had a $R^2 > 0.9$ and were considered to produce daily mean air temperature maps. Similarly, daily linear regression between altitude and snow thickness (cm) for winter period between 1st January - 10th June 2018 and 27th October – 31st December 2018 were extrapolated to obtain mean snow thickness maps. Both the maps were carried out using the Raster calculator in ArcGIS Pro 2.7. The snow thickness was corrected for slope and curvature like in Guglielmin and Testa (2003) called Snow Accumulation Factor (SAF) and concavity-convexity factor (CCF). The snow regression model was converted into snow presence/absence during winter. In summer, snow presence/absence was obtained through the supervised classification of PlanetScope images (single snow band) with random forest algorithm (misclassification error of 3.42 % compared to the regression model) when the lapse-rate regressions were not statistically significant because of the patchy and negligible snow cover that is not represented by 6 widespread AWSs. We used PlanetScope images resampled to match the DEM resolution, because, among satellite platforms, it has a high spatial and temporal resolution (3.0 m on daily basis) making it highly effective for daily monitoring over local regions. Several polygons were digitized to represent classes of snow and snow-free areas. Afterwards, 50 random points were generated, and a confusion matrix was calculated per each of 10 different dates, well distributed across summer (Aberle et al., 2024).

Consistently with the PERMACLIM model assumptions, we considered the GST to be 0 °C when snow cover was present. This is crucial because the stored ground heat accumulated during summer turns into approximately 0 °C at the surface in presence of the snow cover. This is particularly true for this study area and period: the average winter (snow-covered) GST for the 37 ground thermistors was 0.1 ± 0.35 °C. Conversely, while in snow-free conditions of PERMACLIM GST was assumed to correspond to air temperature (AT) (GST = AT) (Guglielmin and Testa, 2003; Guglielmin et al., 2022; Paro et al., 2014), here instead we incorporated the influence of potential solar radiation on GST (Abramov et al., 2008; Guglielmin et al., 2008) using the Area Solar Radiation tool in ArcGIS Pro 2.7. Specifically, based on the linear regression of few GSTs in the study area with potential solar radiation, for the months of July, August, and September, we applied Eq. (1), while for June Eq. (2) was employed:

$$GST = 0.0015*RAD - 5.7848 + AT \quad (1)$$

$$GST = 0.0018*RAD - 7.897 + AT \quad (2)$$

where *RAD* is the potential cumulative solar radiation of the day and *AT* is the daily air temperature.

Finally daily GST values were used to compute the annual TDD used in the active layer model following the methodology shown in Fig. 4.

4.2. Active Layer model

In our study we employed two types of Stefan's solution depending on the availability of input data (ALT1 and ALT2). The first one is expressed in Eq. (3) as:

$$ALT1 = E\sqrt{TDD_s} \quad (3)$$

Where TDDs are ground surface TDD (°C day) calculated by summing values above 0 °C from daily GST obtained using the cell statistics tool in ArcGIS Pro 2.7 and E is the edaphic factor (Nelson and Outcalt, 1987) without the n-factor (Hinkel and Nicholas, 1995; Romanovsky and Osterkamp, 1997; Wilhelm et al., 2015; Kurylyk and Hayashi, 2016; Hrbáček and Uxa, 2020) (Eq. (4)):

$$E1 = \sqrt{\frac{2k_t}{P_b wL}} \quad (4)$$

where k_t is thermal conductivity of the ground ($Wm^{-1}K^{-1}$), P_b is the soil density ($kg\ m^{-3}$), w is the moisture content ($kg\ kg^{-1}$) and, L is the latent heat of fusion (333,660 J kg^{-1}) (Ponti et al., 2024). The second version of the Stefan's solution is expressed in Eq. (5) as:

$$ALT2 = E\sqrt{TDD_a} \quad (5)$$

where TDDa are air TDD (calculated by summing values above 0 °C from the daily Air Temperature dataset using the cell statistics tool in ArcGIS Pro 2.7) and, therefore, the addition of the n-factor (useful to assess the ground temperature in case of absence of GST) (Zhang et al., 2005; Xu and Wu, 2021) is necessary with in the edaphic factor formula (Eq. (6)), that is:

$$E2 = \sqrt{\frac{2k_t n_t}{P_b wL}} \quad (6)$$

Where n_t is the average n-factor of thaw (unitless) (Zhang et al., 2005) that was obtained dividing the TDDs of the 37 ground surface temperature points by the TDDa deriving from the adjacent AWS air temperature recording daily values.

The thermal conductivity of the material was achieved by the reclassified geological map from 24 classes (Montrasio et al., 2012) to 7 classes according to their lithology as reported in Table 1. Thermal conductivity, density and porosity of the rock types were taken from literature or measured (refer to Table 1).

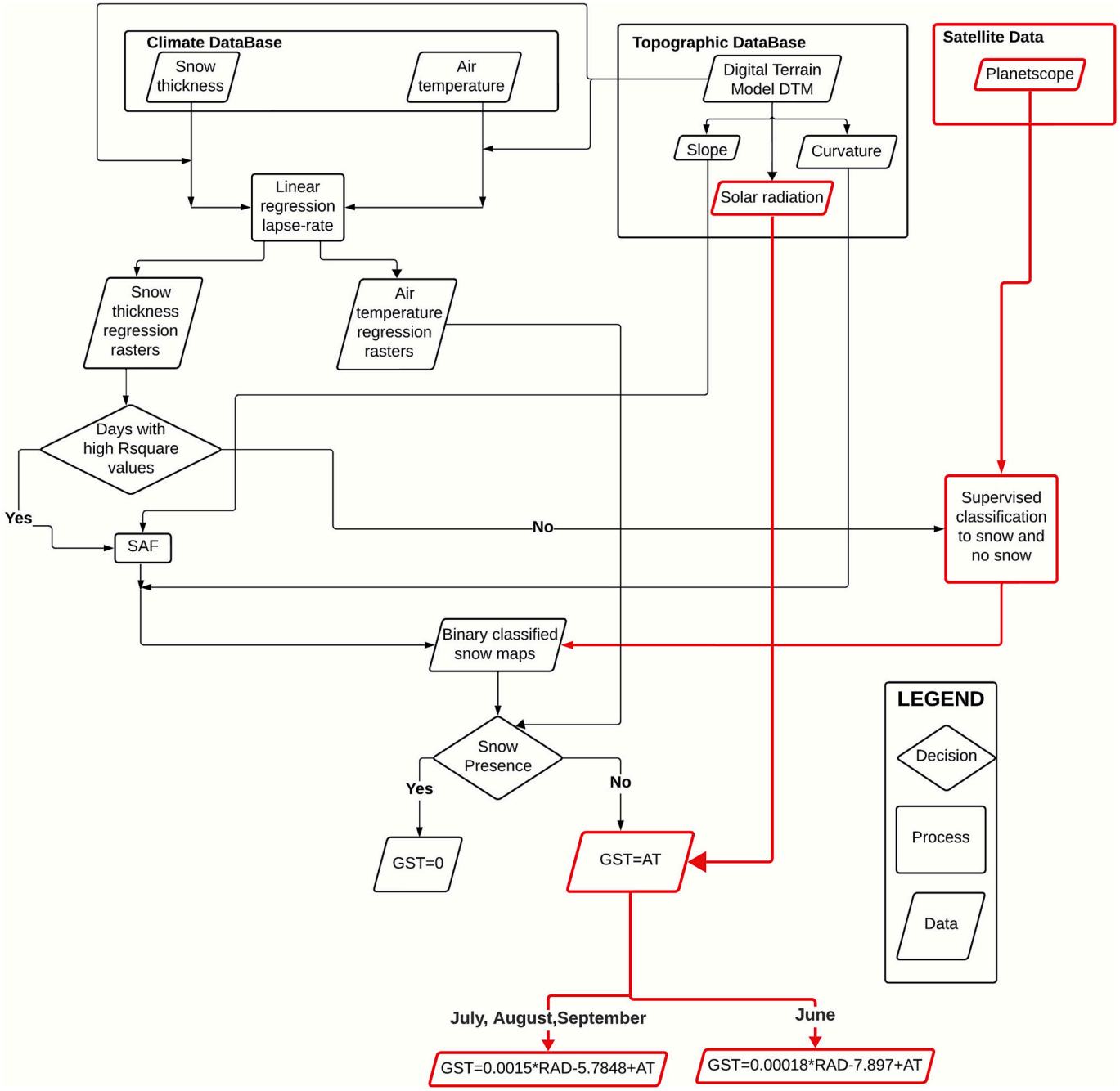

Fig. 4. Methodology chart for modelled GST. In red all the improvements respect the original model PERMACLIM (Guglielmin and Testa, 2003). (For interpretation of the references to colour in this figure legend, the reader is referred to the web version of this article.)

The water content for each bedrock or deposit with different lithology was estimated through a direct proportion equation between the maximum and minimum Topographic Wetness Index (TWI) value (Sørensen et al., 2006; Riihimäki et al., 2021) computed through the hydrology module of SAGA GIS (v.8.5.1) and the measured (or published) (Table 1) highest and lowest values of the deposit water content (or porosity of rocks) with a resolution of 5 m. The validation of this simple regression was made through the root mean square error (RMSE) between modelled and observed data for the lithologies that hosted more than 2 samples. The obtained average RMSE was 13.5 %.

The updated model has been applied only where permafrost occurs according to the permafrost map of the Alpine Permafrost Index Model (APIM, Boeckli et al., 2012) independently from the permafrost probability.

The model accuracy performance for the modelled GST, snow thickness, snow coverage, and ALT was assessed based on RMSE (Chai and Draxler, 2014), determination coefficient R^2 (Asuero et al., 2006) and *p* value. Moreover, the modelled ALT classes were tested for statistical difference through an ANOVA analysis.

5. Results

5.1. Thawing degree days

The modelled TDDs reflected mainly the elevation (decreasing with the increase of the altitude) with the higher values mostly concentrated at the lower elevations (coloured in yellow), and the lower TDDs values at the higher altitude (coloured in blue) (Fig. 5a). Similar pattern

Table 1
Lithological classes with their conductivity, density and porosity (or WC for deposit) values.

Lithology	Thermal Conductivity (Wm^{-1} K^{-1})	Density (Kg m^{-3})	Porosity or Water Content (for deposits) (Min-Max %)
Dolostone	4.5 (Guglielmin et al., 2018)	2700 (Arisona et al., 2018)	0–20 (Singhal and Gupta, 2010; Jasim et al., 2019)
Limestone with clay	1.9 (Manuel et al., 2016; Miao and Zhou, 2017)	2380 (Schueler and Holland, 2000; Arisona et al., 2018)	0–25 (Singhal and Gupta, 2010; Jasim et al., 2019)
Paragneiss	3.5 (Ray et al., 2006)	2630 (Šamalikova, 1983; Tenzer et al., 2011)	0–1 (measured)
Mafic granulite	2.4 (Ray et al., 2006)	2885 (Motta et al., 2017)	0–1.1 (Ray et al., 2015)
Ortogneiss	5.1 (Ray et al., 2006)	2700 (Giacomini et al., 2009; Tenzer et al., 2011)	0–0.5 (measured)
Sandy gravel with soil	1.4 (Markle et al., 2006; Manuel et al., 2016)	1973 (StructX Densities of Different Soil Types, 2025; Arisona et al., 2018)	17–54 (measured)
Gravel blocky sand without soil	2.2 (Markle et al., 2006; Manuel et al., 2016)	2219 (Schueler and Holland, 2000; Tenzer et al., 2011; Arisona et al., 2018)	14–40 (measured)

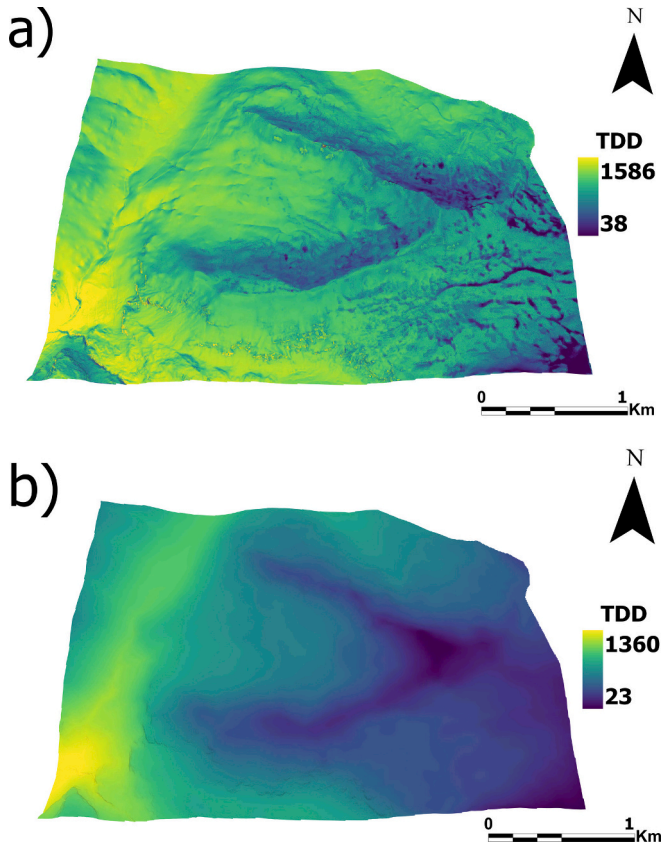

Fig. 5. Spatial distribution of TDDs from modelled GSTs (a) and TDDs obtained through air temperatures (TDDa) multiplied by the n-factor. GSTs obtained from the improvement of PERMACLIM accounted for the solar radiation correction during summer. Areas in yellow depict higher values of TDD while areas in blue show lower values. (For interpretation of the references to colour in this figure legend, the reader is referred to the web version of this article.)

occurred with TDDa multiplied by the n-factor (representing calculated TDDs) although showing lower values both at the lowest and highest elevations (Fig. 5b).

5.2. Snow thickness

As a proof that snow thickness (presence) through lapse-rate linear regression during summer is not suitable, in Fig. 6a it is shown the snow thickness distribution obtained from the linear regression that is much more widespread than what is truly visible using the PlanetScope images (Fig. 6b) during summer. Therefore, relying on all year round on the lapse-rate regression could have underestimated the GST (because where snow is present the GST is 0 °C).

Fig. 6c, instead, shows snow thickness for a winter date with lapse-rate regression (28/02/2018) that indicates as the steepest slopes could be almost snow free or with a thin snow cover even in the middle of the winter.

The summer snow falls are accurately depicted using PlanetScope image classification (orange and green vertical lines), perfectly matching the pattern of snow thickness recorded from the AWS (dark blue line) as showed in Fig. 7.

Validation for SAF-corrected snow thickness shows a RMSE value of 16.40 cm and a high R^2 value of 0.9 denoting high efficiency of the model prediction during winter if compared with an AWS (ITEX Stelvio Pass). In addition, the percentage of misclassified pixels between PlanetScope and ground observed snow cover over a period of 117 summer days shows a high accuracy of classification (3.4 %) (Table 2).

5.3. Ground surface temperature

Our findings reveal a statistically significant and robust variability of GST, as validated by field observations ($R^2 = 0.9$ for both points, p value <0.05 and p value <0.1 for both points) (Fig. 8). The ground validation of the modelled GST was performed using data from two ground-measured points selected based on data completeness and elevation, as illustrated in Fig. 3. These points are located on the southern and northern slopes within the study area (refer to Fig. 1d). The high coefficient of determination ($R^2 = 0.9$) shows the model's efficacy in capturing GST variability during the summer period despite of a slight average underestimation of the modelled values in summer accounting for 0.45 and 0.51 °C for ITEX Stelvio Pass and ITEX Scorluzzo, respectively.

5.4. Active layer thickness

The computation of ALT has been set within the boundaries of all favourable conditions of permafrost according Boeckli et al. (2012) and results differently if ALT1 or ALT2 are applied. In particular, ALT1 ranges between less than 1 m to more than 7.5 m, with no discernible correlation with altitude (Fig. 9a) with the highest occurrence (48 %) between 1 and 2 m range, followed by 2 to 3 m (39 %). ALT2 is less thick, between 1 and 2 m range (13 %) while the highest percentage (44 %) falls between 2 and 3 m range (Fig. 9b). The ground validation for the modelled ALT1 and ALT2 was carried out on nine points located in Fig. 1d. ALT1 shows significantly good relation following an R^2 and low RMSE value (0.93, 0.32 m) for modelled active layer thickness with ERT profiles Table 3.

6. Discussion

6.1. Active layer thickness

ALT can be calculated from a variety of equations such as Kudryavtsev (Riseborough et al., 2008; Li et al., 2022), COUP model (Hollesen et al., 2011; Rasmussen et al., 2017), CryoGrid2 (Westermann et al., 2017a, 2017b), CryoGrid3 (Westermann et al., 2016), GIPL2-MPI

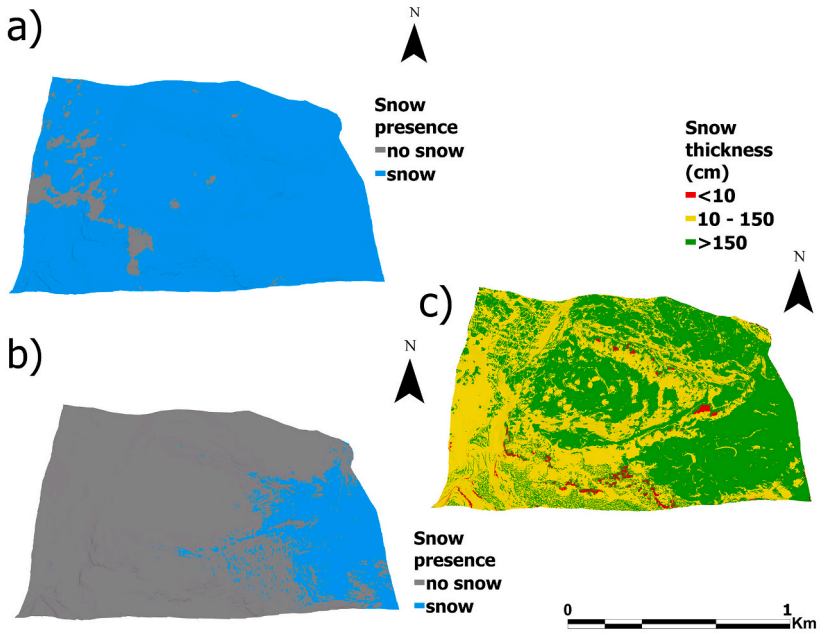

Fig. 6. Snow thickness and presence in the Stelvio area: a) lapse-rate regression snow presence map calculated for summer period (01/09/2018), b) PlanetScope classified snow presence map for summer period (01/09/2018) and c) lapse-rate regression snow thickness corrected with SAF and curvature effect for winter period (28/02/2018).

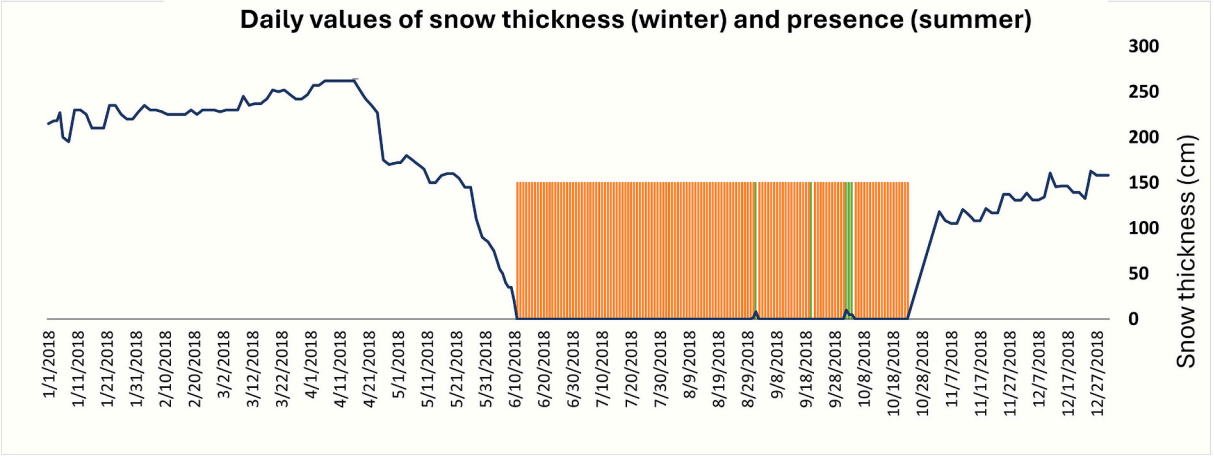

Fig. 7. Comparison between snow presence derived from PlanetScope (summer) and recorded by AWS (ITEX Stelvio Pass) (winter) for a single location at the centre and well representative of the study area. Green lines represent the classified presence of snow (PlanetScope), orange line shows classified value of snow absence (PlanetScope) and blue line depicts snow thickness in cm observed throughout the at the AWS point. (For interpretation of the references to colour in this figure legend, the reader is referred to the web version of this article.)

Table 2
Accuracy table for a) snow presence modelled via PlanetScope classification, b) lapse-rate linear regression vs observed presence (AWS) in 2018 for a single location (ITEX Stelvio Pass), and c) confusion matrix of the classification method.

	Misclassified days	R^2	Total of days	Misclassification (%)	RMSE (cm)	Overall accuracy (%)	Cohen's K
a) PlanetScope vs AWS (summer)	4		117	3.42			
b) Snow elevation regression vs AWS (winter)		0.9	247		16.4		
c) Random forest classification quality (summer)			10 on 117			90–96	0.76–0.91

(Jafarov et al., 2012). Most of these models require a substantial number of site-specific parameters and many calculation parameters. This pre-requisite has impeded the advancement of methodologies aimed at assessing the thickness of the active layer across extensive regions and imposing great uncertainty making them complex for local-level studies (Nelson et al., 1997; Xu and Wu, 2021). Hence, Stefan's solution is the simplest model that can relate ground thermal regime to climate with a smaller number of site-specific parameters to map ALT (Zhang et al., 2024).

The significance of seasonal fluctuations in snow cover on the ground thermal regime, impacting ALT, has been well-documented (Pogliotti et al., 2015; Xu and Wu, 2021). Our study reinforces this finding through

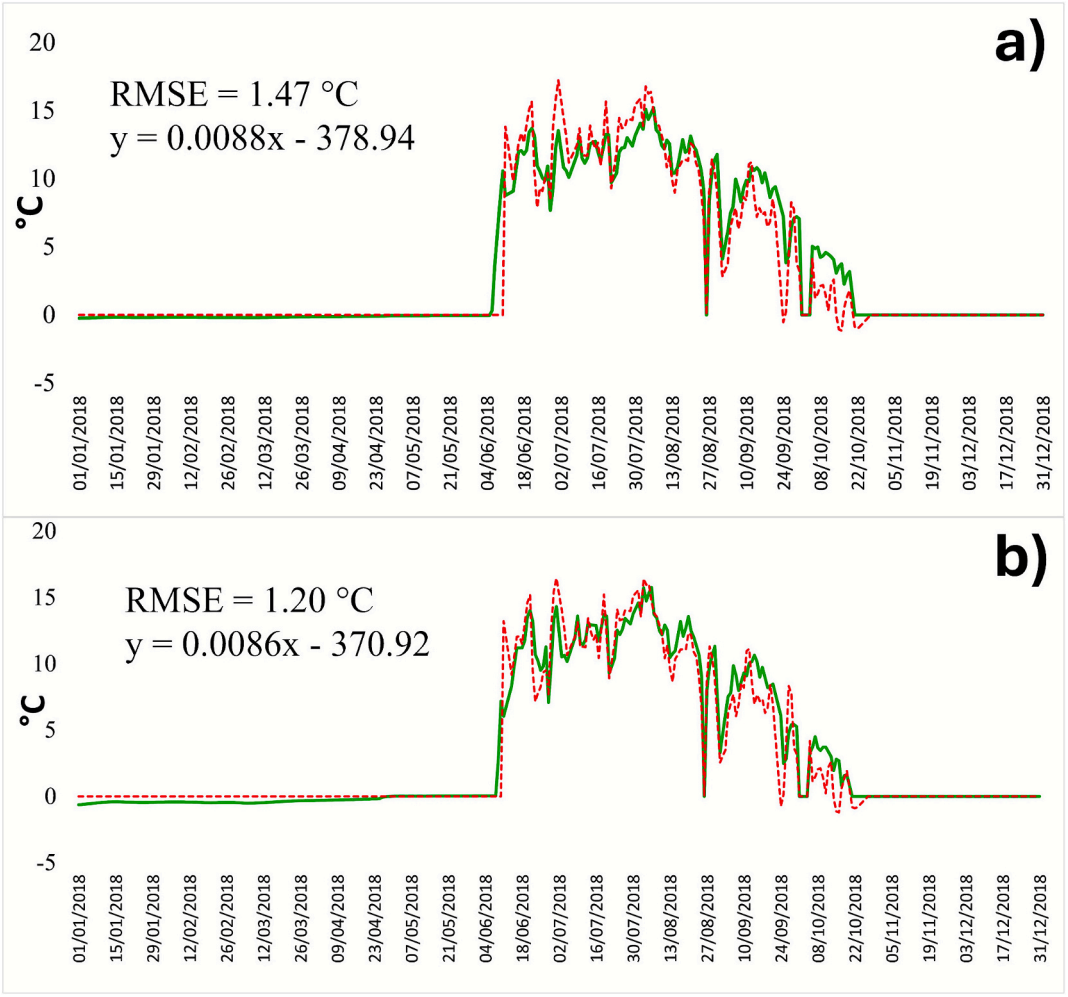

Fig. 8. Linear comparison graph of daily observed GST values (green solid line) at ITEX Stelvio Pass and ITEX Scorluzzo (see Fig. 1d) versus modelled values (red dashed line). It is possible to see that, despite a statistically significant and strong linear regression, there is a slight overall underestimation of the modelled values. (For interpretation of the references to colour in this figure legend, the reader is referred to the web version of this article.)

modelling observations, revealing that snow cover simulated during both winter and summer seasons has a discernible effect on daily ground surface temperatures. These temperature variations serve as crucial input variables for ALT mapping. Moreover, our investigation underscores the pivotal role of ground properties in governing active layer dynamics (Outcalt et al., 1990; Nelson et al., 1997). Local-scale ALT variability is strongly influenced by factors such as water content (Hilbich et al., 2008) and lithological properties (Smith and Riseborough, 2002; Hrbáček and Uxa, 2020). These findings are visually depicted in Fig. 9 illustrating analogous patterns of ALT variability in response to changes in ground properties.

Comparing ALT1 and ALT2, the former demonstrates better performance due to the integration of GST, which has been refined by accounting for factors such as winter snow thickness, summer snow presence/absence, wind effect (CCF), slope (SAF) and potential solar radiation. (Ponti et al., 2024).

The fact that ALT2 validation gave a higher RMSE value (1.36 m) is presumably due to the use of the n-factor with TDDa. Indeed, although this solution is widely used in absence of surface temperatures (Xu and Wu, 2021; Zhang et al., 2024), even a good representativeness of n-factors could not explain the high spatial variability of the snow cover duration and thickness if averaged. As a consequence, the use of an average n-factor is not suggested and gives worse results for ALT modelling as already demonstrated (Ponti et al., 2024). The number of ERT profiles could seem low, but it should be considered that only profiles belonging to the same year of the model and laying on the APIM has been considered. To support the apparently limited validation, the SSB extrapolation of ALT for 2018 (different method) indicated a value of 3.6 m (Table 3). The difference of 1.2 m might be large, but the location of SSB on dolostone with average WC of <5 % (Guglielmin et al., 2018) and the peculiar lower accumulation of snow on that windy ridge could explain the potential difference.

When comparing ALT across all permafrost APIM classes (Table 4), ALT2 shows a higher proportion of thinner active layers (< 3 m). Notably, in both ALT models, the percentage of dominant ALT classes increases as the permafrost probability decreases. For instance, in ALT1, the dominant thickness range of 2–3 m rises from 38 % in areas classified as present permafrost to 51 % in the less probable permafrost class. This outcome is expected, as the APIM framework suggests that lower permafrost probability typically corresponds to less favourable conditions for permafrost formation, which would generally imply a thicker active layer (Yi et al., 2018). Conversely, for $1 < ALT < 2$ m the trend is opposite, thus less coverage of this class for low permafrost probability. It is likely that these 2 ALT classes could be indicators and discriminators of ground surface warm and cold conditions.

In our case, within each ALT class, the TDDs distribution impacts permafrost probability more than any other factors used in the Stefan's equation as thermal conductivity, density or water content. Indeed, the range and mean of TDDs increase from presence to less favourable permafrost at each ALT class as can be seen in Table 5 and showed by the

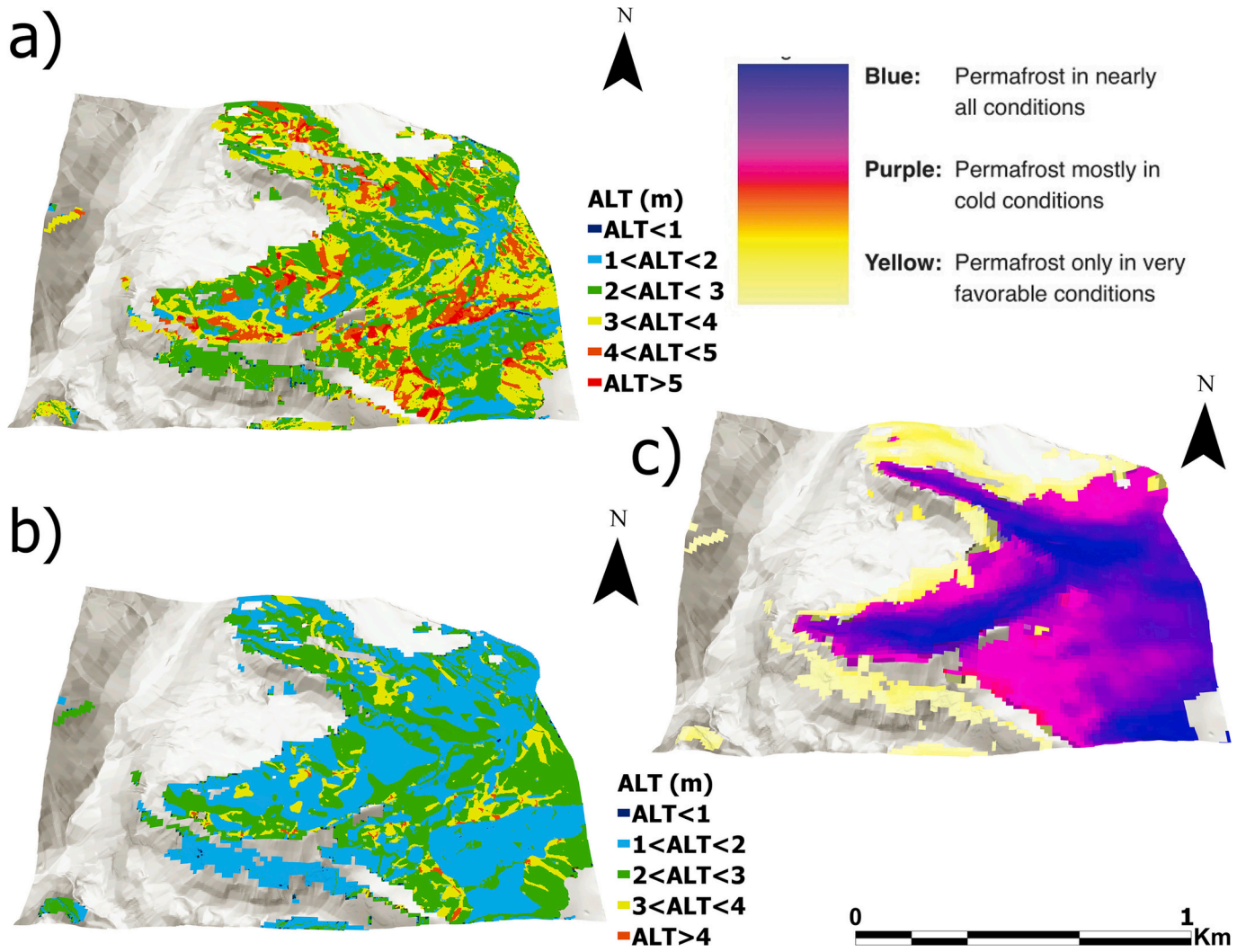

Fig. 9. 3D Comparison map of ALT from our updated PERMACLIM model: a) ALT1: obtained through Stefan's Equation using surface TDDs (Eqs. (3) and (4); b) ALT2: obtained through TDDa with n-factor and edaphic factor (Eqs. (5), and (6); c) Alpine Permafrost Index Map (APIM, Boeckli et al., 2012). Legend: blue-violet = present; pink = probable; yellow = less probable). (For interpretation of the references to colour in this figure legend, the reader is referred to the web version of this article.)

Table 3
Comparison of observed ALT obtained through electrical resistivity tomography (ERT) profiles with modelled ALT1 and ALT2. Please note that SSB corresponds to the closest (180 m) borehole to the study area showed in Fig. 1. The extrapolated ALT (Guglielmin, 2006) was compared with the pixels average ALT of the 2 models.

Point number	Observed ALT (m)	Modelled ALT1 (m)	Modelled ALT2 (m)
ERT1	3.8	3.7	2.5
ERT2	4.1	3.9	2.8
ERT3	3.8	3.5	2.3
ERT4	3.4	2.9	2.4
ERT5	3.2	2.8	2.5
ERT6	4.1	3.6	2.6
ERT7	4.5	4.6	2.9
ERT8	4.2	3.9	3.0
ERT9	4.6	4.8	2.8
		RMSE 0.32	**RMSE** 1.36
		$\mathbf{R^2}$ 0.93	$\mathbf{R^2}$ 0.58
SSB	3.6	2.4	1.8

frost number in another study (Hrbáček et al., 2020). On the other hand, Despite a general increase of TTDs from thinner to thicker ALT classes, TDDs do not always increase with increasing ALT. Indeed, in some cases such as ALT between 4 and 5 m in the less probable permafrost class of APIM and ALT >5 m in the probable permafrost class, the higher thermal conductivity increases the ALT despite lower TDDs (compared to thinner ALT classes). This pattern indicates that, especially for higher TDDs values, thermal conductivity becomes very relevant, and this is particularly challenging in the ALT modelling of the deposits because thermal conductivity depends not only on the mineralogical and petrographical properties but also on the porosity that is highly variable in deposits. In addition, also density increased in these classes, suggesting that possibly the ground heat flux can penetrate to deeper layers more easily at such densities of the material and higher thermal conductivity. However, ANOVA analysis suggests that average TDDs are not statistically significant in discriminating all the ALT classes (F-value = 0.9, $p = 0.5$). Rather, other factors contributing to the model gave a statistical contribution, such as Kt (F-value = 28.2, $p < 0.001$), soil density (F-value = 20.4, $p < 0.001$) and WC (F-value = 84.9, $p < 0.001$) (Table 5).

6.2. *Advantages and limitations*

Our model demonstrated that incorporating daily estimates of GST alongside the presence or absence of summer snow effectively mitigated

Table 4
Spatial distribution of ALT (%) per permafrost class (a) ALT1 estimated with modelled TDDs and, (b) ALT2 estimated using n-factor and edaphic factor.

	APIM Permafrost class	ALT class	Percentage (%)
a) ALT1	Present	ALT<1	0.1
		1 < ALT<2	22.6
		2 < ALT<3	37.8
		3 < ALT<4	29.2
		4 < ALT<5	9.1
		ALT>5	1.2
b) ALT1	Probable	ALT<1	0.0
		1 < ALT<2	6.2
		2 < ALT<3	49.8
		3 < ALT<4	28.8
		4 < ALT<5	11.4
		ALT>5	3.7
c) ALT1	Less Probable	ALT<1	0.0
		1 < ALT<2	2.7
		2 < ALT<3	51.3
		3 < ALT<4	33.1
		4 < ALT<5	10.5
		ALT>5	2.4
a) ALT2	Present	ALT<1	0.0
		1 < ALT<2	45.6
		2 < ALT<3	44.7
		3 < ALT<4	9.3
		ALT>4	0.3
b) ALT2	Probable	ALT<1	0.0
		1 < ALT<2	52.5
		2 < ALT<3	39.1
		3 < ALT<4	7.6
		ALT>4	0.9
c) ALT2	Less Probable	ALT<1	0.1
		1 < ALT<2	58.5
		2 < ALT<3	34.9
		3 < ALT<4	6.3
		ALT>4	0.2

instances of AWS failure to detect summer snowfall, thereby enhancing the predictive accuracy of GST and permafrost (Langer et al., 2010; Zhang et al., 2020). On the other hand, the high variability of cloudiness in this area could have altered the increase of GST respect to the air temperature, as it is possible to see in Fig. 8, where an underestimation is visible especially in the second half of summer. This is due to the fact that the Area Solar Radiation tool in ArcGIS presets standard values for the diffuse proportion, transmissivity and the diffuse model type parameters. This might have deviated the potential solar radiation from the real solar radiation and, in a future research, the above-mentioned parameters should be adapted to the local cloudiness.

Furthermore, the PERMACLIM model assumes that snow thickness $\geq$ 80 cm insulates the ground (Guglielmin and Testa, 2003; Ponti et al., 2021), whereas here we did not consider thickness, rather the presence of snow to provide insulation in summer period. This assumption treats snow cover as a homogenous layer, thereby affecting the accuracy of ground thermal regime estimates. However, as visible in Fig. 10, the snow-free season have a few days with negative mean daily air temperature (less than 10 % at the highest elevation and averagely less than 4 % in the rest of the area). Therefore, generally, it is possible to assume that the bottom temperature of the snowpack during summer is always around 0 °C because of the snow melting during the snow-free season (Guglielmin and Testa, 2003).

We need also to underline that a possible inaccuracy of the calculation of ALT using Stefan's equation is related to the values of thermal parameters when adopted from literature sources without field analysis, except for dolostone (Guglielmin et al., 2018). However, by adopting an uncertainty value of 10 % of the thermo-physical parameters, it was possible to run a quantitative assessment of the ALT. For the 2 validation points of Fig. 8 it is visible how minimizing and maximizing kt and Pb by 10 %, a range of ALT of 2.66–3.25 (modelled value of 2.94) and 1.98–2.42 m (modelled value of 2.19 m) is visible for ITEX Stelvio Pass and ITEX Scorluzzo, respectively. This is not a large difference and, therefore, a generous confidence interval could also be accepted for the data obtained by literature.

Additionally, water content calculations were based on a direct proportion equation with TWI with calculations only performed for points within 5 out of 7 lithological classes, introducing uncertainty into ALT estimation, even though TWI has been proved to be a key parameter (Pandey et al., 2023). However, a RMSE of 13.5 % seems reasonable for the assessment of WC through the TWI in this heterogeneous area. Indeed, the application of such an interval for WC would produce an ALT

Table 5
Ranges and mean values of TDDs and of the other parameters used in the Stefan's equation in the case of ALT1 model: thermal conductivity (k_t, W m^{-1} K^{-1}), density (P_b, kg m^{-3}) and water content (WC, kg kg^{-1}) for all the classes of ALT in the different classes of permafrost according APIM. Bold ALT classes shows when the thermal conductivity impacts more than TDDs in the ALT definition.

APIM classes	ALT class range (m)	TDD range (°C day)	TDD mean (°C day)	K_t range (W m^{-1} K^{-1})	K_t mean (W m^{-1} K^{-1})	P_b range (kg m^{-3})	P_b mean (kg m^{-3})	WC Range (kg kg^{-1})	WC Mean (kg kg^{-1})
Present		38.87–820.21	170.6	1.89–4.5	2.34	2219–2700	2256.51	0.01–0.19	0.07
Probable		nodata	no data	2.20–2.20	2.2	2219–2219	2219	no data	no data
Less probable	< 1	818.54–1116.26	990.9	1.89–1.89	1.89	2380–2380	2380	0.01–0.02	0.01
Present		69.50–1012.02	654.17	1.39–5.09	2.28	1973–2700	2241.38	0.02–0.2	0.07
Probable	1–2	192.31–1075.02	851.96	1.39–5.09	2.15	1973–2885	2209.07	0.03–0.13	0.06
Less probable		515.32–1224.59	947.85	1.39–4.5	2.19	1973–2700	2265.03	0.02–0.11	0.05
Present		38.87–1048.38	731.6	1.39–5.09	3.31	917–2885	2395.48	0.04–0.25	0.11
Probable		192.31–1095.45	910.66	1.39–5.09	2.79	1973–2885	2238.95	0.04–0.31	0.11
Less probable	2–3	475.87–1355.77	991.32	0.60–5.09	2.58	1973–2885	2191.68	0.04–0.23	0.11
Present		337.44–1040.77	761.24	1.39–5.09	4.22	917–2885	2659.8	0.08–0.38	0.15
Probable		433.56–1094.65	923.76	1.39–5.09	3.17	1973–2885	2506.09	0.07–0.41	0.17
Less probable	3–4	594.04–1326.46	995.63	0.60–5.09	2.91	997–2885	2396.25	0.07–0.34	0.16
Present		384.56–1047.08	830.53	1.39–5.09	4.69	917–2700	2695.18	0.13–0.46	0.2
Probable		452.90–1095.43	925.66	1.39–5.09	4.35	1973–2885	2657.71	0.12–0.47	0.2
Less probable	4–5	561.47–1276.96	970.55	0.60–5.09	4.27	997–2700	2646.14	0.12–0.46	0.19
Present		574.59–1034.86	890.38	2.20–5.09	4.66	2219–2700	2697.55	0.2–0.46	0.29
Probable		514.79–1063.48	921.4	3.5–5.09	4.61	2630–2700	2697.72	0.2–0.52	0.29
Less probable	> 5	632.57–1104.55	1004.99	3.5–5.09	4.57	2630–2700	2679.41	0.18–0.55	0.26

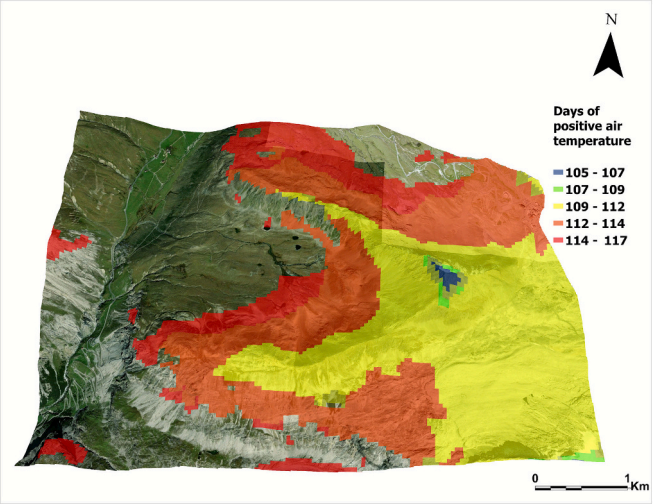

Fig. 10. Spatialization of the number of days with positive daily mean air temperature throughout the entire snow-free period in which the linear regressions for the snow distribution are not applicable (117 days between early June and early October). It is possible to see that even at the highest elevation less than 10 % of the days have negative air temperature.

range of 2.42–4.08 and 1.7–3.75 m for ITEX Stelvio Pass and ITEX Scorluzzo, respectively. This remains in line with what considered ALT in this sector of the Alps (Guglielmin et al., 2018; Ponti et al., 2024).

Lastly, a high-resolution Digital Terrain Model (DTM) could potentially improve model resolution in the future and no suitable DTM currently exists for the study area.

7. Conclusions

In this study, we updated the PERMACLIM model to delineate the ALT in the vicinity of Stelvio Pass, located in the Italian Alps. Our enhancements include a higher temporal resolution for air temperature and snow cover thickness, calculated daily rather than monthly, which is particularly significant during the Spring and Fall. Additionally, unlike PERMACLIM, we included presence or absence of snow cover during the summer to account for cooling events that, on a monthly temporal resolution, would not have been depicted. Even more importantly, the inclusion of the potential solar radiation in the calculation of GST and thus TDDs helped to get closer to real surface temperature values that, in any case, could not be equal to the air temperature.

Here we demonstrated that ALT1 has better predictive accuracy, yielding an RMSE of 0.32 m, whereas the ALT2 1.36 m, thereby validating the enhanced efficacy of TDDs instead of TDDa with n-factors. Our results demonstrate that the dominant ALT range (2–3 m) spatially increases with the decrease in permafrost favourability classes within APIM, correctly suggesting warmer conditions. Moreover, we found that generally the summer GST and therefore TDDs are the main driver of the ALT, although thermal conductivity can be the leading parameter especially for the higher TDDs values.

CRediT authorship contribution statement

Vasudha Chaturvedi: Writing – original draft, Formal analysis, Data curation. **Stefano Ponti:** Writing – review & editing, Supervision, Methodology, Conceptualization. **Mauro Guglielmin:** Writing – review & editing, Supervision, Methodology, Conceptualization.

Declaration of competing interest

The authors declare that they have no known competing financial interests or personal relationships that could have appeared to influence the work reported in this paper.

Data availability

Data will be made available on request.

References

Aberle, R., Enderlin, E., O'Neel, S., Florentine, C., Sass, L., Dickson, A., Marshall, H.P., Flores, A., 2024. Dataset for automated snow cover detection on mountain glaciers using space-borne imagery. The Cryosphere 19, 1675–1693. https://doi.org/10.5194/tc-19-1675-2025.

Abramov, A., Gruber, S., Gilichinsky, D., 2008. Mountain permafrost on active volcanoes: Field data and statistical mapping, Klyuchevskaya Volcano group, Kamchatka, Russia. Permafrost and Periglacial Processes 19, 261–277. https://doi.org/10.1002/PPP.622.

Arisona, A., Nawawi, M., Khalil, A.E., Abdulrahman, A., 2018. Assessment of microgravity anomalies of soil structure for geotechnical 2D models. Journal of Geoscience, Engineering, Environment, and Technology 3, 151–154.

Asuero, A.G., Sayago, A., González, A.G., 2006. The correlation coefficient: an overview. Critical Reviews in Analytical Chemistry 36, 41–59.

Biskaborn, B.K., Smith, S.L., Noetzli, J., Matthes, H., Vieira, G., Streletskiy, D.A., Schoeneich, P., Romanovsky, V.E., Lewkowicz, A.G., Abramov, A., Allard, M., 2019. Permafrost is warming at a global scale. Nature Communications 10 (1), 264. https://doi.org/10.1038/s41467-018-08240-4.

Boeckli, L., Brenning, A., Gruber, S., Noetzli, J., 2012. Permafrost distribution in the European Alps: calculation and evaluation of an index map and summary statistics. The Cryosphere 6, 807–820. https://doi.org/10.5194/tc-6-807-2012.

Cannone, N., Sgorbati, S., Guglielmin, 2007. Unexpected impacts of climate change on alpine vegetation. Frontiers in Ecology and the Environment 5, 360–364. https://doi.org/10.1890/1540-9295(2007)5[360:UIOCCO]2.0.CO;2.

Cannone, N., Guglielmin, Hauck C., Vonder Mühll, D., 2003. The impact of recent glacier fluctuation and human activities on permafrost distribution, Stelvio Pass (Italian Central-Eastern Alps). In: ICOP 2003 - Permafrost 1, pp. 125–130 https://doi.org/ISBN 90 5809 582 7.

Chai, T., Draxler, R.R., 2014. Root mean square error (RMSE) or mean absolute error (MAE)? Geoscientific Model Development 7, 1525–1534. https://doi.org/10.5194/gmdd-7-1525-2014.

Etzelmüller, B., Guglielmin, M., Hauck, C., Hilbich, C., Hoelzle, M., Isaksen, K., Noetzli, J., Oliva, M., Ramos, M., 2020. Twenty years of European mountain permafrost dynamics-the PACE legacy. Environmental Research Letters 15, 104070. https://doi.org/10.1088/1748-9326/abae9d.

Fisher, J.P., Estop-Aragonés, C., Thierry, A., Charman, D.J., Wolfe, S.A., Hartley, I.P., Murton, J.B., Williams, M., Phoenix, G.K., 2016. The influence of vegetation and soil characteristics on active-layer thickness of permafrost soils in boreal forest. Global Change Biology 22, 3127–3140. https://doi.org/10.1111/GCB.13248.

Gardner, W.H., 1986. Water content. In: Arnold, K. (Ed.), Methods of Soil Analysis: Part 1 Physical and Mineralogical Methods, 2nd ed. SSSA Book Series, pp. 493–544.

Giacomini, A., Buzzi, O., Renard, B., Giani, G.P., 2009. Experimental studies on fragmentation of rock falls on impact with rock surfaces. International Journal of Rock Mechanics and Mining Sciences 46, 708–715. https://doi.org/10.1016/J.IJRMMS.2008.09.007.

Gruber, S., Haeberli, W., 2007. Permafrost in steep bedrock slopes and its temperature-related destabilization following climate change. Journal of Geophysical Research 112, F02S18. https://doi.org/10.1029/2006JF000547.

Guglielmin, M., 2006. Ground surface temperature (GST), active layer and permafrost monitoring in continental Antarctica. Permafrost and Periglacial Processes 17, 133–143. https://doi.org/10.1002/ppp.553.

Guglielmin, Aldighieri B., Testa, B., 2003. PERMACLIM: a model for the distribution of mountain permafrost, based on climatic observations. Geomorphology 51, 245–257. https://doi.org/10.1016/S0169-555X(02)00221-0.

Guglielmin, M., Cannone, N., Dramis, F., 2001. Permafrost–glacial evolution during the Holocene in the Italian Central Alps. Permafrost and Periglacial Processes 12, 111–124. https://doi.org/10.1002/ppp.379.

Guglielmin, M., Ellis Evans, C.J., Cannone, N., 2008. Active layer thermal regime under different vegetation conditions in permafrost areas. A case study at Signy Island (Maritime Antarctica). Geoderma 144, 73–85. https://doi.org/10.1016/j.geoderma.2007.10.010.

Guglielmin, Donatelli M., Semplice, M., Capizzano, S.S., 2018. Ground surface temperature reconstruction for the last 500 years obtained from permafrost temperatures observed in the SHARE STELVIO Borehole, Italian Alps. Climate of the Past 14, 709–724. https://doi.org/10.5194/cp-14-709-2018.

Guglielmin, M., Ponti, S., Forte, E., Cannone, N., 2021. Recent thermokarst evolution in the Italian Central Alps. Permafrost and Periglacial Processes 32, 299–317. https://doi.org/10.1002/ppp.2099.

Guglielmin, Bonasera M., Fubelli, G., Tellini, C., Dramis, F., 2022. Permafrost-based geomorphology of the Mt. Foscagno - Mt. Forcellina ridge (Adda – Inn River basins, Central Italian Alps). Journal of Maps 18, 441–447. https://doi.org/10.1080/17445647.2022.2082331.

Heijmans, M.M.P.D., Magnússon, R., Lara, M.J., Frost, G.V., Myers-Smith, I.H., van Huissteden, J., Jorgenson, M.T., Fedorov, A.N., Epstein, H.E., Lawrence, D.M., Limpens, J., 2022. Tundra vegetation change and impacts on permafrost. Nature Reviews Earth & Environment 13, 68–84. https://doi.org/10.1038/s43017-021-00233-0.

Hilbich, C., Hauck, C., Hoelzle, M., Scherler, M., Schudel, L., Völksch, I., Vonder Mühll, D., Mäusbacher, R., 2008. Monitoring mountain permafrost evolution using electrical resistivity tomography: a 7-year study of seasonal, annual, and long-term variations at Schilthorn, Swiss Alps. Journal of Geophysical Research: Earth Surface 113. https://doi.org/10.1029/2007JF000799.

Hinkel, K.M., Nicholas, J.R.J., 1995. Active layer thaw rate at a boreal forest site in Central Alaska. Arctic and Alpine Research 27, 72–80. https://doi.org/10.1080/00040851.1995.12003098.

Hjort, J., Streletskiy, D., Doré, G., Wu, Q., Bjella, K., Luoto, M., 2022. Impacts of permafrost degradation on infrastructure. Nature Reviews Earth & Environment 3, 24–38.

Hoelzle, M., Mittaz, C., Etzelmüller, B., Haeberli, W., 2001. Surface energy fluxes and distribution models of permafrost in European mountain areas: an overview of current developments. Permafrost and Periglacial Processes 12, 53–68. https://doi.org/10.1002/ppp 385.

Hollesen, H., Elberling, B., Janssons, P.E., 2011. Future active layer dynamics and carbon dioxide production from thawing permafrost layers in Northeast Greenland. Global Change Biology 17, 911–926. https://doi.org/10.1111/j.1365-2486.2010.02256.x.

Hrbáček, F., Uxa, T., 2020. The evolution of a near-surface ground thermal regime and modeled active-layer thickness on James Ross Island, Eastern Antarctic Peninsula, in 2006–2016. Permafrost and Periglacial Processes 31, 141–155. https://doi.org/10.1002/ppp.2018.

Hrbáček, F., Oliva, M., Fernández, J.R., Kňažková, M., de Pablo, M.A., 2020. Modelling ground thermal regime in bordering (dis)continuous permafrost environments. Environmental Research 181, 108901. https://doi.org/10.1016/j.envres.2019.108901.

Jafarov, E.E., Marchenko, S.S., Romanovsky, V.E., 2012. Numerical modeling of permafrost dynamics in Alaska using a high spatial resolution dataset. The Cryosphere 6, 613–624. https://doi.org/10.5194/tc-6-613-2012.

Jasim, A., Hemmings, B., Mayer, K., Scheu, B., 2019. Groundwater flow and volcanic unrest. Advances in Volcanology 83–99. https://doi.org/10.1007/11157_2018_33.

Jiang, G., Fu, Z., Gao, S., Zhao, H., Chen, J., Liu, Y., Wu, Q., 2024. Long-term responses of permafrost to the dual impacts of climate warming and engineering disturbance along the Qinghai-Tibet Highway. Cold Region Science and Technololy 220, 104135. https://doi.org/10.1016/J.COLDREGIONS.2024.104135.

Keller, F., 1992. Automated mapping of mountain permafrost using the program PERMAKART within the geographical information system ARC/INFO. Permafrost and Periglacial Processes 3 (2), 133–138. https://doi.org/10.1002/ppp.3430030210.

Kurylyk, B.L., Hayashi, M., 2016. Improved Stefan equation correction factors to accommodate sensible heat storage during soil freezing or thawing. Permafrost and Periglacial Processes 27, 189–203. https://doi.org/10.1002/PPP.1865.

Langer, M., Westermann, S., Boike, J., 2010. Spatial and temporal variations of summer surface temperatures of wet polygonal tundra in Siberia - implications for MODIS LST based permafrost monitoring. Remote Sensing of Environment 114, 2059–2069. https://doi.org/10.1016/j.rse.2010.04.012.

Li, G., Zhang, M., Pei, W., Melnikov, A., Khristoforov, I., Li, R., Yu, F., 2022. Changes in permafrost extent and active layer thickness in the Northern Hemisphere from 1969 to 2018. Science of the Total Environment 804, 150182. https://doi.org/10.1016/J.SCITOTENV.2021.150182.

Liu, Y., Wang, X., Wen, Y., Cai, H., Song, X., Zhang, Z., 2024. Effects of freeze-thaw cycles on soil greenhouse gas emissions: a systematic review. Environmental Research 248, 118386. https://doi.org/10.1016/j.envres.2024.118386.

Malfasi, F., Cannone, N., 2020. Climate warming persistence triggered tree ingression after shrub encroachment in a High Alpine Tundra. Ecosystems 23, 1657–1675. https://doi.org/10.1007/s10021-020-00495-7.

Malfasi, F., Cannone, N., 2021. Phytosociology of the vegetation communities of the Stelvio Pass area. Journal of Maps 17, 367–375. https://doi.org/10.1080/17445647.2021.1957033.

Manuel, J., Márquez, A., Bohórquez, M.Á.M., Melgar, S.G., 2016. Ground thermal diffusivity calculation by direct soil temperature measurement. Application to very Low Enthalpy Geothermal Energy Systems. Sensors 16, 306. https://doi.org/10.3390/s16030306.

Markle, J.M., Schincariol, R.A., Sass, J.H., Molson, J.W., 2006. Characterizing the two-dimensional thermal conductivity distribution in a sand and gravel aquifer. Soil Science Society of America Journal 70, 1281–1294. https://doi.org/10.2136/SSSAJ2005.0293.

Miao, S., Zhou, Y., 2017. Temperature dependence of thermal diffusivity and conductivity for sandstone and carbonate rocks. Journal of Thermal Analysis and Calorimetry 131, 1647–1652. https://doi.org/10.1007/s10973-017-6631-7.

Montrasio, A., Berra, F., Cariboni, M., Ceriani, M., Deichmann, N., Ferliga, C., Gregnanin, A., Guerra, S., Gugliemin, M., Jadoul, F., Longhin, M., 2012. CARG - Carta geologica nazionale scala 1:50.000 - Note illustrative del Foglio geologico 024 BORMIO, p. 120.

Motta, Gabriel J., Morales, N., Malagutti, W., 2017. Geophysical perspective on the structural interference zone along the Neoproterozoic Brasília and Ribeira fold belts in West Gondwana. Brazilian Journal of Geology 47, 3–19.

Mourey, J., Marcuzzi, M., Ravanel, L., Pallandre, F., 2019. Effects of climate change on high Alpine mountain environments: evolution of mountaineering routes in the Mont Blanc massif (Western Alps) over half a century. Arctic, Antarctic and Alpine Research 51, 176–189. https://doi.org/10.1080/15230430.2019.1612216.

Nelson, F.E., Outcalt, S.I., 1987. A computational method for prediction and regionalization of permafrost. Arctic and Alpine Research 19, 279–288. https://doi.org/10.1080/00040851.1987.12002602.

Nelson, F.E., Shiklomanov, N.I., Mueller, G.R., 1997. Estimating active-layer thickness over a large Region: Kuparuk River Basin, Alaska, U.S.A. Arctic and Alpine Research 29, 367–378.

Outcalt, S.I., Nelson, F.E., Hinkel, K.M., 1990. The Zero-curtain effect-heat and mass transfer across an isothermal region in freezing soil. Water Resources Research 26, 1509–1516. https://doi.org/10.1029/WR026i007p01509.

Pandey, A., Yadav, B.C., Wani, J.M., Dimri, A.P., 2023. Permafrost estimation model in Upper Indus Basin. Journal of Earth System Science 132. https://doi.org/10.1007/s12040-023-02176-0.

Paro, L., Pispico, R., Ronchi, C.H., Provenzale, M., Colombo, N., 2014. PERMACLIM model implementation in QuantumGIS software: a new open source tool to simulate the spatial distribution of alpine permafrost. Huggel C, Krautblatter M, Hewitt K (eds). GAPHAZ List of Abstracts.

Pogliotti, P., Guglielmin, M., Cremonese, E., Morra di Cella, U., Filippa, G., Pellet, C., Hauck, C., 2015. Warming permafrost and active layer variability at Cime Bianche, Western European Alps. The Cryosphere 9, 647–661. https://doi.org/10.5194/tc-9-647-2015.

Ponti, S., Cannone, N., Guglielmin, M., Guglielmin, 2021. A new simple topo-climatic model to predict surface displacement in paraglacial and periglacial mountains of the European Alps: the importance of ground heating index and floristic components as ecological indicators. Ecological Indicators 120, 106889. https://doi.org/10.1016/J.ECOLIND.2020.106889.

Ponti, S., Girola, I., Guglielmin, M., 2024. Thermal photogrammetry on a permafrost rock wall for the active layer monitoring. Science of the Total Environment 917, 170391. https://doi.org/10.1016/j.scitotenv.2024.170391.

Ran, Y., Li, X., Cheng, G., Che, J., Aalto, J., Karjalainen, O., Hjort, J., Luoto, M., Jin, H., Obu, J., Hori, M., 2022. New high-resolution estimates of the permafrost thermal state and hydrothermal conditions over the Northern Hemisphere. Earth System Science Data 14, 865–884. https://doi.org/10.5194/essd-14-865-2022.

Rasmussen, L.H., Zhang, W., Hollesen, J., Cable, S., Christiansen, H.H., Jansson, P.E., Elberling, B., 2017. Modelling present and future permafrost thermal regimes in Northeast Greenland. Cold Regions Science and Technology 146, 199–213. https://doi.org/10.1016/j.coldregions.2017.10.011.

Ray, L., Förster, H.J., Schilling, F.R., Förster, A., 2006. Thermal diffusivity of felsic to mafic granulites at elevated temperatures. Earth and Planetetary Science Letters 251, 241–253. https://doi.org/10.1016/J.EPSL.2006.09.010.

Ray, L., Förster, H.J., Förster, A., Fuchs, S., Naumann, R., Appelt, O., 2015. Tracking the thermal properties of the lower continental crust: Measured versus calculated thermal conductivity of high-grade metamorphic rocks (Southern Granulite Province, India). Geothermics 55, 138–149. https://doi.org/10.1016/j.geothermics.2015.01.007.

Riihimäki, H., Kemppinen, J., Kopecký, M., Luoto, M., 2021. Topographic wetness index as a proxy for soil moisture: the importance of flow-routing algorithm and grid resolution. Water Resources Research 57, e2021WR029871. https://doi.org/10.1029/2021WR029871.

Riseborough, D., Shiklomanov, N., Etzelmüller, B., Gruber, S., Marchenko, S., 2008. Recent advances in permafrost modelling. Permafrost and Periglacial Processes 19, 137–156.

Romanovsky, V.E., Osterkamp, T.E., 1997. Thawing of the active layer on the coastal plain of the Alaskan Arctic. Permafrostost and Periglacial Processes 8, 1–22. https://doi.org/10.1002/(SICI)1099-1530(199701)8:1.

Šamalikova, M., 1983. Scanning electron microscopy examples of clay residua from crystalline rocks. Bulletin of Engineering Geology & the Environment 28, 91–102.

Schueler, T., Holland, H.K., 2000. Soil physical properties and processes - Minnesota Stormwater Manual. Watershed Protection Techniques 3, 661–665.

Schuur, E.A.G., McGuire, A.D., Schädel, C., Grosse, G., Harden, J.W., Hayes, D.J., Hugelius, G., Koven, C.D., Kuhry, P., Lawrence, D.M., Natali, S.M., 2015. Climate change and the permafrost carbon feedback. Nature 520, 171–179. https://doi.org/10.1038/nature14338.

Singhal, B.B.S., Gupta, R.P., 2010. Applied Hydrogeology of Fractured Rocks, Second edition. Springer Science & Business Media, pp. 1–408. https://doi.org/10.1007/978-90-481-8799-7.

Smith, M.W., Riseborough, D.W., 2002. Climate and the limits of permafrost: a zonal analysis. Permafrost and Periglacial Processes 13, 1–15. https://doi.org/10.1002/ppp.410.

Song, X., Wang, G., Ran, F., Huang, K., Sun, J., Song, C., 2020. Soil moisture as a key factor in carbon release from thawing permafrost in a boreal forest. Geoderma 357, 113975. https://doi.org/10.1016/J.GEODERMA.2019.113975.

Sørensen, R., Zinko, U., Seibert, J., 2006. On the calculation of the topographic wetness index: evaluation of different methods based on field observations. Hydrology and Earth System Sciences 10, 101–112. https://doi.org/10.5194/hess-10-101-2006.

Stocker-Mittaz, C., Hoelzle, M., Haeberli, W., 2002. Modelling alpine permafrost distribution based on energy-balance data: a first step. Permafrost and Periglacial Processes 13 (4), 271–282. https://doi.org/10.1002/ppp.426.

StructX Densities of Different Soil Types, 2025. https://structx.com/Soil_Properties_002.html.

Tenzer, R., Sirguey, P., Rattenbury, M., Nicolson, J., 2011. A digital rock density map of New Zealand. Computers and Geosciences 37, 1181–1191. https://doi.org/10.1016/j.cageo.2010.07.010.

Wang, K., Jafarov, E., Overeem, I., 2020. Sensitivity evaluation of the Kudryavtsev permafrost model. Science of The Total Environment 720, 137538. https://doi.org/10.1016/J.SCITOTENV.2020.137538.

Wani, J.M., Thayyen, R.J., Ojha, C.S.P., Gruber, S., 2021. The surface energy balance in a cold and arid permafrost environment, Ladakh, Himalayas, India. The Cryosphere 15, 2273–2293. https://doi.org/10.5194/tc-15-2273-2021.

Westermann, S., Langer, M., Boike, J., Heikenfeld, M., Peter, M., Etzelmüller, B., Krinner, G., 2016. Simulating the thermal regime and thaw processes of ice-rich permafrost ground with the land-surface model CryoGrid 3. Geoscientific Model Development 9, 523–546. https://doi.org/10.5194/gmd-9-523-2016.

Westermann, S., Elberling, B., Pedersen, S.H., Stendel, M., Hansen, B.U., Liston, G.E., 2017a. Future permafrost conditions along environmental gradients in Zackenberg, Greenland. The Cryosphere 9, 719–735. https://doi.org/10.5194/tc-9-719-2015.

Westermann, S., Peter, M., Langer, M., Schwamborn, G., Schirrmeister, L., Etzelmüller, B., Boike, J., 2017b. Transient modeling of the ground thermal conditions using satellite data in the Lena River delta, Siberia. The Cryosphere 11, 1441–1463. https://doi.org/10.5194/TC-11-1441-2017.

Wilhelm, K.R., Bockheim, J.G., Kung, S., 2015. Active layer thickness prediction on the Western Antarctic Peninsula. Permafrost and Periglacial Processes 26, 188–199. https://doi.org/10.1002/ppp.1845.

Woo, M.K., Kane, D.L., Carey, S.K., Yang, D., 2008. Progress in permafrost hydrology in the new millennium. Permafrost and Periglacial Processes 19, 237–254. https://doi.org/10.1002/ppp.613.

Wu, Q., Ma, W., Lai, Y., Cheng, G., 2024. Permafrost degradation threatening the Qinghai–Xizang Railway. Engineering. https://doi.org/10.1016/J.ENG.2024.01.023.

Xu, X., Wu, Q., 2021. Active layer thickness variation on the Qinghai-Tibetan Plateau: historical and projected trends. Journal of Geophysical Research: Atmospheres 126. https://doi.org/10.1029/2021JD034841.

Yi, Y., Kimball, J.S., Chen, R.H., Moghaddam, M., Reichle, R.H., Mishra, U., Zona, D., Oechel, W.C., 2018. Characterizing permafrost active layer dynamics and sensitivity to landscape spatial heterogeneity in Alaska. The Cryosphere 12, 145–161. https://doi.org/10.5194/tc-12-145-2018.

Yi, Y., Kimball, J.S., Chen, R.H., Moghaddam, M., Miller, C.E., 2019. Sensitivity of active-layer freezing process to snow cover in Arctic Alaska. The Cryosphere 13, 197–218. https://doi.org/10.5194/tc-13-197-2019.

Zhang, T., Frauenfeld, O.W., Serreze, M.C., Etringer, A., Oelke, C., McCreight, J., Barry, R.G., Gilichinsky, D., Yang, D., Ye, H., Ling, F., 2005. Spatial and temporal variability in active layer thickness over the Russian Arctic drainage basin. Journal of Geophysical Research D: Atmospheres 110, 1–14. https://doi.org/10.1029/2004JD005642.

Zhang, Y., Qian, B., Hong, G., 2020. A long-term, 1-km resolution daily meteorological dataset for modeling and mapping permafrost in Canada. Atmosphere 11. https://doi.org/10.3390/atmos11121363.

Zhang, C., Douglas, T.A., Brodylo, D., Bosche, L.V., Jorgenson, M.T., 2024. Combining a climate-permafrost model with fine resolution remote sensor products to quantify active-layer thickness at local scales Combining a climate-permafrost model with fine resolution remote sensor products to quantify active-layer thickness at loca. Environmental Research Letters 19, 44030. https://doi.org/10.1088/1748-9326/ad31dc.